Stack pressure dependence on the three-dimensional structure of a composite electrode in an all-solid-state battery

Yuya Sakka[a], Hisao Yamashige [b], Akihisa Takeuchi[c], Masayuki Uesugi[c], Kentaro Uesugi[c] and Yuki Orikasa*[a]

[a] Department of Applied Chemistry, Ritsumeikan University, 1-1-1 Nojihigashi, Kusatsu, Shiga 525-8577, Japan.

[b] Toyota Motor Corporation, Toyota-cho, Toyota, Aichi 471-8571, Japan

[c] Japan Synchrotron Radiation Research Institute, 1-1-1 Kouto, Sayo, Hyogo 679-5198, Japan.

*orikasa@fc.ritsumei.ac.jp

Abstract:

An all-solid-state battery in which the organic liquid electrolyte of a lithium-ion battery (LIB) is replaced with an inorganic solid electrolyte is a candidate for next-generation rechargeable batteries. Although the solid electrolyte has high conductivity, the charge and discharge characteristics are inferior to those of conventional LIBs. To achieve the high performance of all-solid-state batteries, it is necessary to grasp the phenomena peculiar to the composite electrode that uses the solid electrolyte. This study analyses the three-dimensional structure of the composite electrode in an all-solid-state battery using a laboratory-built cell capable of performing electrochemical and X-ray computed tomography (CT) measurements while monitoring stack pressures. The dependencies of stack pressure on the porosity, contact area, and tortuosity of the composite electrodes are quantitatively analysed to evaluate their effects on the electrochemical properties. The CT observation reveals that there is insufficient contact between the active material and the solid electrolyte in a plane perpendicular to the pressure direction. The contact interface is found to be a key parameter for the charge/discharge characteristics.

Introduction

An all-solid-state battery (ASSB) using an inorganic solid electrolyte (SE) is expected to be safer than a conventional lithium-ion battery (LIB) equipped with an organic liquid electrolyte [1]. Furthermore, when a SE with a transport number of one is used, it is hardly affected by variation in the electrolyte salt concentration, which is a problem for liquid electrolytes [2-5], and this improves the rate capability [6]. In addition, mechanically suppressing the dendrite formation that occurs in lithium metal anodes potentially raises the energy density [7, 8]. However, despite the discovery of SEs with high ionic conductivity [9], in general the charge/discharge performance of all-solid-state batteries is lower than that observed in liquid electrolytes. In order to make the most of the advantages of ASSB, it is necessary to understand the reaction mechanism within the electrode.

Since the electrochemical reaction of batteries proceeds at the two-dimensional electrode–electrolyte interface [10], a composite electrode, which is a mixture of an active material (AM), an electrolyte, and a conductive additive, is used as the electrode of an ASSB to increase the effective reaction area. The available supply of ions and electrons in the composite electrode greatly affects the energy density, rate capability, and cycling performance of an ASSB. The ion and electron passes are related to the microstructure of the composite electrode [11], and they depend on the engineering fabrication conditions, such as composition [12-14], external press pressure [15], binder [16], *etc*. In LIBs using liquid electrolytes, the AM and electrolyte form an essentially sufficient interfacial connection. In contrast, in an ASSB, when the contacts between the AM and SE happen to be poor, the transportation of ions is restricted [17-20]. In other words, for an ASSB, as well as the challenge of maximising the ion-transport pathways in composite electrodes, which it shares with LIBs, there is the added challenge of ensuring solid-to-solid contacts, and both of these challenges need to be overcome.

Not only is high pressure applied during the preparation of ASSB electrodes, but pressure must be maintained during the charge/discharge reactions. The former is the fabrication pressure and the latter is the stack pressure. The parameters of the pressure have a direct effect on the void fraction in the composite electrode and change the apparent ionic conductivity [21-23]. Stack pressure is necessary to maintain proper contact between the electrode and the SE. To optimise the performance of an ASSB, it is necessary to understand the effect of the stacking pressure on it. Previous studies on the correlation between stack pressure and the three-dimensional structure at the lithium anode and SE interface have shown that dendrite formation occurs at higher stack pressures [24, 25]. On the cathode side, it has been shown that strain caused by the pressure reduces the contact between the AM and SE and determines the performance [17, 22].

Analysis of the three-dimensional structure has been carried out using focused-ion-beam scanning electron microscopy (FIB-SEM) [15, 26] and X-ray computed tomography (CT) [23, 27-31]. In particular, in X-ray CT, there is the advantage that operando measurement can be performed while changing the pressure or allowing electrochemical measurement to proceed. This has already been shown to be useful for dendrite observation in SE [27-31] and electrode structure analysis of AM/SE [17]. The three-dimensional structure from X-ray CT data can be combined with the simulation to discuss the

inhomogeneous charge/discharge mechanism[32]. Although it has become widely known that the pressure of an ASSB affects the three-dimensional structure, quantitative analysis of the cathode three-dimensional structure controlled by stacking pressure, and direct observation of the anisotropy of the contact interface do not yet appear to have been fully explored. In this study, a cell capable of electrochemical and X-ray CT measurements is developed while controlling the stack pressure of an ASSB, and the dependency of the stack pressure on the three-dimensional structure of a cathode is quantified. It is directly observed that the contact between AM and SE is anisotropic with respect to the pressure, which is a phenomenon peculiar to ASSB.

Experimental terms

The cathode AM, SE, and conductive agent were $LiNbO_3$-coated $LiNi_{0.33}Co_{0.33}Mn_{0.33}O_2$ (NCM), $Li_{10}GeP_2S_{12}$ (LGPS), and acetylene black (DENKA BKACK, Denka Co., Ltd.) (AB), respectively. The coating was applied using a rolling fluidised coating machine (MP-01, Powrex) based on a procedure previously described in the literature [33]. The LGPS was prepared via a solid-state reaction at 550 °C under an Ar flow. The scanning electron micrograph of NCM and LGPS are provided as Figs. S1 and S2 in the supporting information. These were mixed in a mortar in a glove box in an Ar atmosphere at a ratio of 1:1:0.1 by mass. For the anode, an In-Li alloy was formed by crimping an In foil (Nilaco) with a Li foil (Honjo Metal Co., Ltd.). The 1.0 mg of cathode composite, 2.5 mg of electrolyte, and In-Li foil were placed in a cylinder with a diameter of 1 mm. The inside of the cylinder was sealed with an O-ring during the measurements. The stack pressure was controlled using screws at the top of the cell. The In-Li | LGPS | NCM all-solid-state cells were placed under five different pressures, namely 6, 12, 25, 50, and 100 MPa with different constraining pressures, and were charged and discharged. The charge/discharge measurements of the prepared In-Li | LGPS | NCM were carried out at 298 K with different stack pressures using a battery test system (HJ1001SDE, Hokuto Denko Co., Ltd.).

The X-ray CT measurements using a monochromatic X-ray beam were performed using beamline BL20XU of SPring-8, Japan with a beam energy of 20 keV. The undulator radiation X-ray beam was diffracted by a Si (111) double-crystal monochromator. The detector was a visible-light conversion type X-ray detector using a CMOS camera (C13440-20CU, Hamamatsu Photonics K. K.) with a pixel size of ca. 0.5 μm and a field of view of ca. 1.0×1.0 mm. For each CT measurement, 1800 projections were collected with a 180° angular range for an exposure time of 0.05 s per frame. Segmentation and analysis of the 3D data were conducted using the Dragonfly 4.1 software (Object Research Systems, Montreal, Canada).

Results and Discussion

An operando X-ray CT measurement cell with monitoring stack pressure is illustrated in Fig. 1. The diameter of the electrode and electrolyte is 1 mm so that the X-ray at 20 keV can penetrate the electrode and electrolyte. These electrodes and electrolyte layers are pushed into the cylinder and pressed using

an upper stainless-steel rod. The rod is also placed on the bottom side, which is contacted with the load-sensing transducer. The upper and bottom rods operate as the current collector. The charge/discharge measurement and X-ray CT measurement can be performed in the same cell while changing the stack pressure.

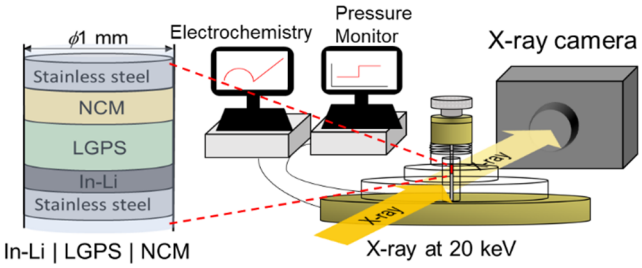

Fig. 1 Illustration of the X-ray CT measurement and an all-solid-state battery cell.

To investigate the relationship between stack pressure and charge/discharge characteristics, two sets of charge/discharge measurements are conducted. The first set is the cycles of charge/discharge measurements with a constant stack pressure of 6 MPa, with the results shown in Fig. 2(a). Because a stack pressure of 6 MPa is very small, both the capacity and cycle performance are low. In the second set, the pressure is increased every two cycles for a total of 10th cycles (Fig. S3). Two cycles of charge/discharge measurements at 6 MPa are first performed, and then two cycles are performed at a stack pressure of 12 MPa. The discharge capacity of the latter measurements is divided by that of the former at the same cycle, which gives the increased capacity deriving from the change in stack pressure. In this study, the loading of NCM is 60 mg cm^{-2}, which is much higher than the reported condition. This is due to the electrode diameter of 1 mm and the readability of the precision electronic balance. The thick composite electrode causes inactive part for charge/discharge. Fig. 2(b) shows a plot of the capacity rate versus the stack pressure as a percentage of the capacity at a 5 MPa stack pressure. A rate of 100% means that there is no change in the capacity at the same number of cycles for the constant pressure condition, and 200% indicates that the capacity is twice the baseline rate (5 MPa) at the increased stack pressure. This value increases logarithmically with respect to the stack pressure.

The previous study has reported that the specific capacity of all-solid-state batteries depends on fabrication pressure, with capacity decreasing at 50 MPa rather than 150 MPa [15]. Since no pressure was added during the fabrication in our experiments, the stack pressure shown in this study corresponds to the previously reported fabrication pressure. In other words, the dependence of charge/discharge capacity on the stack pressure in the range below 100 MPa in this study is consistent with the results of the previous report.

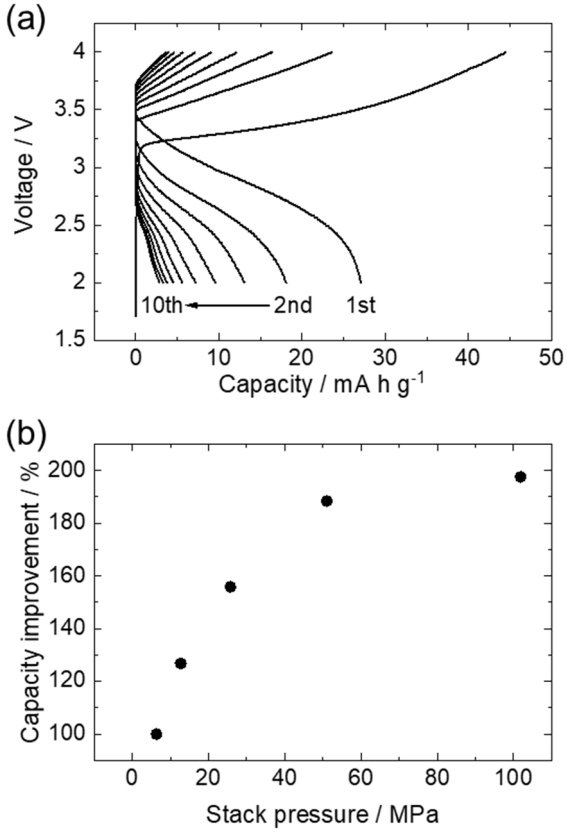

Fig. 2 (a) Charge/discharge cycle curves of an In-Li | LGPS | NCM all-solid-state battery using the laboratory-built measurement cell at a rate of 0.01C and stack pressure of 6 MPa. (b) Capacity improvement versus stack pressure compared with 6 MPa as a baseline.

Next, morphological changes in the composite electrode and the electrolyte under the various stack pressures were analysed using X-ray CT. The reconstructed images of X-ray CT are provided as Figs. S4-S6. The analysed area was 512×512×50 μm^3, which was cropped from the obtained three-dimensional images. The proportions of the NCM, LGPS, and voids were identified based on transmission intensity (Figs. S7-S11). Their volume ratios, NCM/LGPS contact area, and the tortuosity of the LGPS connection pathway into the composite electrode were calculated.

The porosity and contact rate are important parameters involved in Li ion transport in the composite electrode and the effective area of the interfacial reaction between the NCM and LGPS. Fig. 3(a) shows the stack pressure dependence on the porosity of the composite electrode and the SE layer. As the stack pressure increases, the porosity decreases in both, and there is no great difference between the composite electrode layer and the SE layer at stack pressures of less than 12 MPa. However, at high stack pressures, the pressure dependence of the porosity of the composite electrode is reduced. The porosities of the electrode and the electrolyte are 23% and 5% at a pressure of 100 MPa, respectively. There is a large difference between the composite electrode layer and the SE layer at a high stack pressure. This is caused by the presence of the NCM particles, which exhibits a high Young's modulus [34] and large particle size (Fig. S1). Hard NCM particles are slightly deformed by applied pressure and

the NCM particle size is larger than that of LGPS, resulting in more voids around the NCM particles. Fig. 3(b) shows the volume change of the NCM, LGPS, and voids in the composite electrode layer. The proportion of the LGPS decreases while the proportion of the NCMs increases up to a stack pressure of 12 MPa. In composites with different Young's moduli, large pressures can be applied to materials that have larger Young's moduli [23]. NCM particles are preferentially pushed into the measurement space. Hard NCM particles have small deformations in response to stack pressure, and, for uniaxial pressing, high pressure makes LGPS compress around the NCM particles in addition to reducing porosity. This also causes the soft LGPS to contract [35], thus reducing the apparent volume fraction. When the pressure exceeds 12 MPa, the volume of the NCM does not increase, and the porosity decreases due to the increase in the LGPS. The particle size of the NCM particles is on the order of 10 μm, and any increase in the volume ratio levels off due to difficulties in deformation. The LGPS with a smaller grain size and Young's modulus can fill the voids located around the NCMs. Thus, the process of densification in the composite electrode proceeds through two stages.

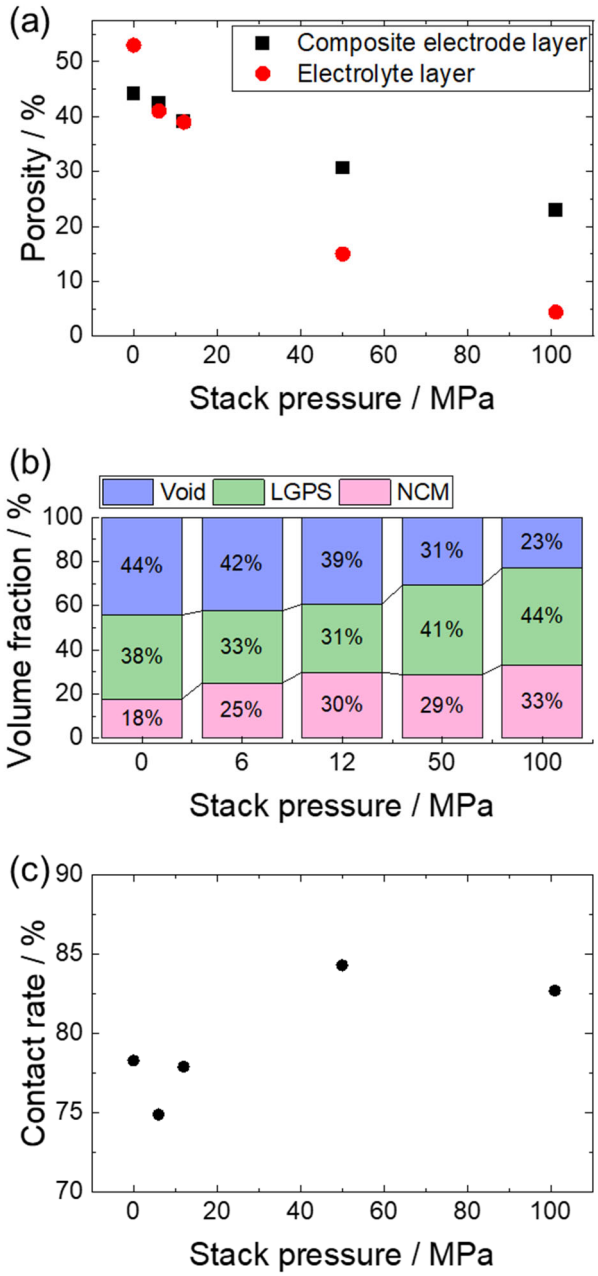

Fig. 3 (a) Stack pressure dependence on the porosity of the composite electrode and SE layer. (b) Volume fraction of the NCM, LGPS, and voids in the composite electrode layer for various stack pressures. (c) Change in the NCM/LGPS contact rate as a function of the stack pressure.

The contact rate represents the fraction of the area contacted between the NCM and LGPS with respect to the surface area of the NCM particles (Fig. S12). The contacted interface between the NCM and LGPS serves as a reactive area for charge-transfer during charge/discharge. Fig. 3(c) shows the change in the NCM/LGPS contact rate as a function of the stack pressure, along with the changes corresponding to the two-stage process described earlier. The rate increases approximately 10% when the stack pressure is greater than 50 MPa compared with the state under stack pressure of less than or

equal to 12 MPa. At low pressures, the NCM particles are pressurised preferentially [22], and so contact with the surrounding LGPS is not increased; however, at high pressures, the LGPS fills the voids around the NCM particles, resulting in an increased contact area. On the other hand, the improvement in the contact rate stopped when pressures reached 50 MPa. After 50 MPa, there are small changes in the volume of the voids, but no change in the contact rate.

During uniaxial pressing, the anisotropy phenomenon occurs within the contacted state between the NCM and LGPS. Fig. 4(a) shows XZ slices highlighting only the contact surface of the NCM particles. Green and blue lines indicate the NMC/LGPS contacted interface and the NCM/void interface, respectively. The relationship between the XZ plane and the pressure direction is shown in Fig. 4(b). The contacted NCM/LGPS interface only serves as a pathway for Li-ion conduction to the AM. Detailed observations of these images reveal that the NCM particles have good contact with the LGPS in the Z-axis direction, which is the pressure direction (Fig. 4(c)). On the other hand, preferential contact with the voids is observed in the horizontal direction, which is not the pressure direction. Such anisotropy of the contacting surface of the NCM is predominantly observed at low pressures, but also even at high pressures, though less frequently. Therefore, it can be concluded that the NCM does not have good contact with the LGPS horizontally, even at high stack pressures. In addition, as shown in Fig. 4(d), many voids in the horizontal direction can be confirmed and the shape of the voids depends on the pressure direction. Therefore, the void formation in the composite electrode and the contacted surface state of the NCM particles corresponds well to the pressure direction.

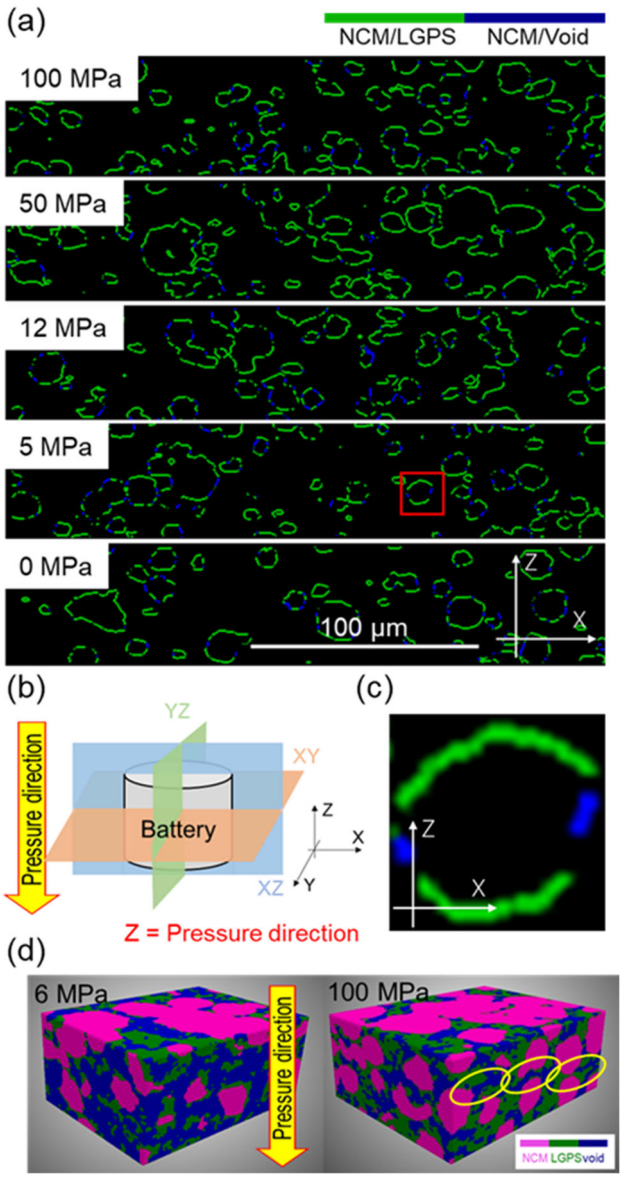

Fig. 4 (a) XZ slices highlighting only the contact surfaces of the NCM particles. Green and blue lines indicate the NMC/LGPS contacted interface and the NCM/void interface, respectively. (b) XYZ axis and pressure direction. (c) Magnified view of the NCM particle at 6 MPa from the red square in (a). (d) Reconstructed three-dimensional image of the composite electrodes at stack pressures of 6 MPa and 100 MPa.

The tortuosity of the lithium-ion pathway in the composite electrode was subsequently calculated. Fig. 5(a) shows the analysed area, which was 36×36×50 μm^3 and cropped from the obtained three-dimensional composite electrode images. In the calculation, a three-dimensional pathway connected by SE particles was extracted in the composite electrode (Fig. 5(a)), and this value was divided by the thickness of the observed region (Fig. 5(b)). Fig. 5(c) shows a histogram of the tortuosity for each stack pressure. Since the reported tortuosity of all-solid-state battery electrodes ranges from 1 to 10 [20, 32, 36-39], this study discuss a relative comparison with the stack pressure. The graph shows the flexural

index on the horizontal axis and the frequency on the vertical axis. The mode value at each pressure value is highlighted with a red circle and the minimum value with a blue circle. Minimum and mode values decrease with increasing pressure. In contrast, when the pressure is 100 MPa, the tortuosity had increased and so had the variation. This mechanism will be discussed later.

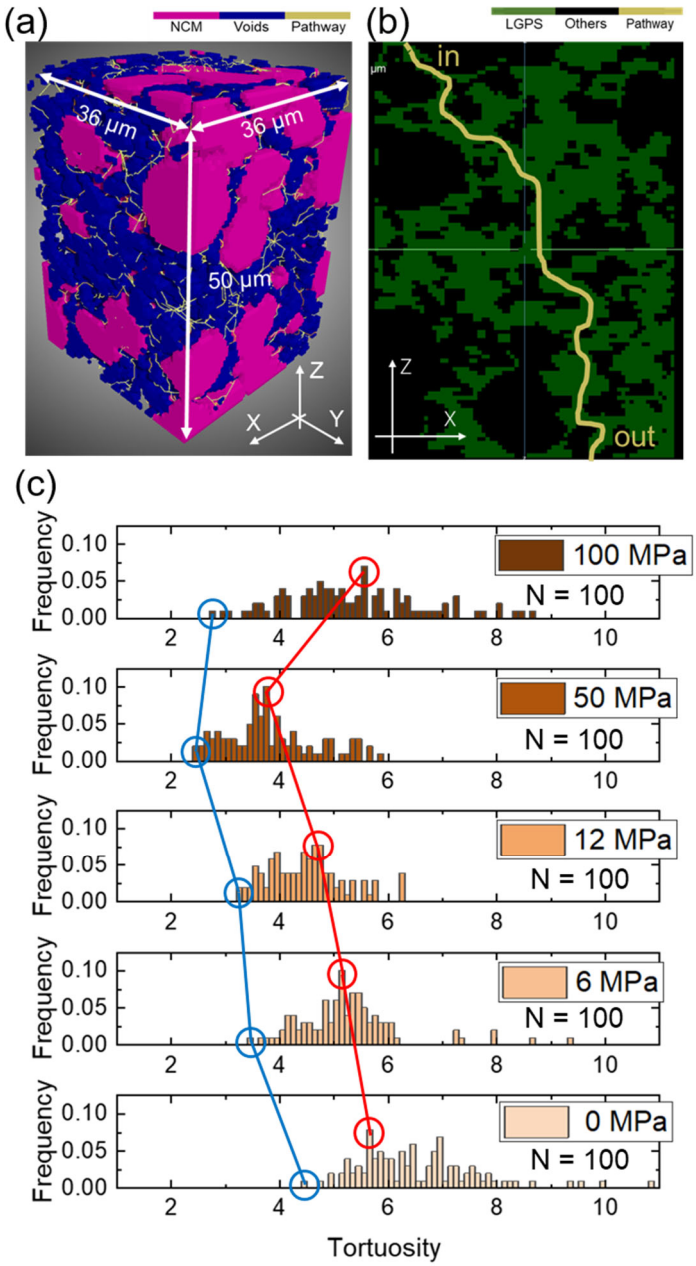

Fig. 5 (a) Cropped part of the obtained three-dimensional composite electrode images used to calculate the tortuosity. (b) Two-dimensional schematic view used to calculate the tortuosity. (c) Histogram of tortuosity for various stack pressures.

The AC impedance measurement was simultaneously performed with the X-ray CT measurements. The stack pressure dependence on the apparent conductivity and the charge-transfer resistance

estimated from the Nyquist plot (Fig. S13 and S14) are provided in Figs. 6(a) and (b), respectively. The apparent conductivity increases almost linearly with increasing stack pressure. This corresponds well to the behaviour of the porosity reduction shown in Fig. 3(a). The analysis of only the SEs has shown that the apparent conductivity increases due to the decrease of the porosity [40] . On the other hand, the charge transfer resistance is inversely proportional to the stack pressure. This corresponds to the increasing of the contact rate of the NCM/LGPS shown in Fig. 3(b). That is, under a high-pressure condition, a good NCM/LGPS interface is formed, which leads to a decrease in the charge-transfer resistance. The increase in the capacity of the charge/discharge reaction (Fig. 1) is mainly attributed to the improved interface between the NCM and LGPS, resulting in a reduction of the charge-transfer resistance.

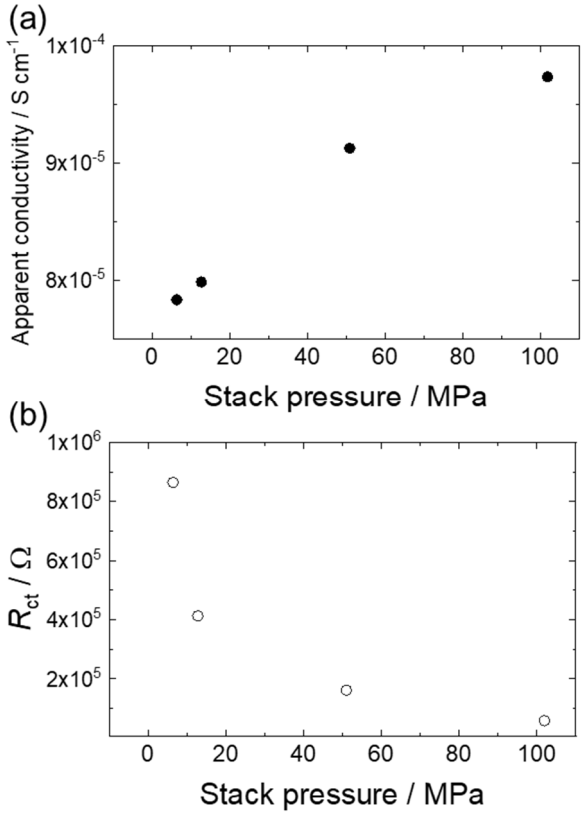

Fig. 6 (a) Apparent conductivity and (b) charge transfer resistance estimated by AC impedance as a function of the stack pressure.

Based on these results, the effects of the AMs in the composite electrode will be discussed. The experimental findings outlined above lead to the morphological changes evident in the pressed composite electrode shown in Fig. 7. Although uniaxial pressing preferentially pushes the NCM particles, owing to their large Young's modulus[34], the pressure of the flat current collector is not sufficiently applied to the space between the AM particles when the AMs are dense. Therefore, low-pressure spots are created in the gaps in the AM, and thus the SE does not fill these gaps, even after pressure is applied. The insufficient contact in the horizontal direction between the AMs and the electrolytes is caused by these low-pressure spots. Since no force is applied from the horizontal

direction, the gap cannot be fully filled. In addition, even where the AMs overlap, the SEs cannot be filled and the voids remain. The unique hardness of the AM causes a difference in the porosity between the composite electrode layer and the SE layer, or else it prevents the composite electrode layers from being kept in contact with each other in the horizontal direction. Under uniaxial pressing, the voids in the composite electrodes that contain AMs have a large Young's modulus that is not sufficiently reduced.

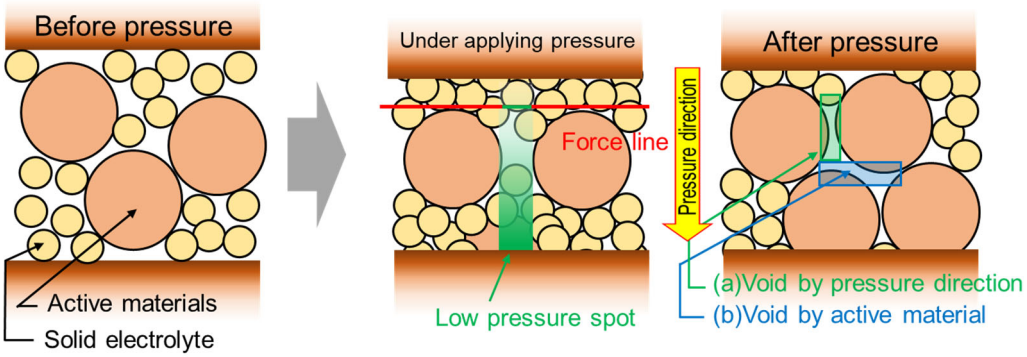

Fig. 7 Schematic illustration of morphological structural changes in a composite electrode from pressure application.

The AMs affect the tortuosity of the composite electrodes. With regard to the stack pressure dependence of the tortuosity, it has been confirmed that the tortuosity increases at 100 MPa. There are two factors that change the tortuosity in composite electrodes: it decreases with the increased volume of the void and increases with the increased volume of the AMs. Both of them exhibit a change in the opposite direction with respect to the stack pressure, and therefore, at the same pressure, the behaviour of the tortuosity is reversed. For small-sized voids, large NCMs act as obstacles in the Li-ion pathway. Therefore, at 100 MPa when the AMs are well filled, the effect of increasing the AM is superior to the effect of decreasing the porosity, resulting in the high tortuosity. The results indicate a reduced change in the minimum value of the tortuosity but do indicate an increase in the average tortuosity. However, it is expected that the increase in the tortuosity will have a minor impact on the electrochemical properties, since the pressure dependence of the charge/discharge measurement does not exhibit significant differences at pressures above 50 MPa.

Conclusions

This study used X-ray computed tomography to analyse the effects of stack pressure on the morphological structure of the composite electrode and electrochemical properties of an all-solid-state battery (ASSB) cell. It was found that increasing the stack pressure decreased the porosity and improved the contact rate between the active material (AM) and the solid electrolyte (SE), while the decrease in porosity impacted the apparent conductivity. The enhanced contact rate between the AM and SE led to an order of magnitude reduction in charge transfer resistance. The logarithmic increase of the charge/discharge capacity with the increase in stack pressure was attributed to both the

improvement in apparent conductivity and the reduction in charge transfer resistance, but the effect of the charge transfer resistance reduction was particularly dominant. The contact interface between the AM and the SE was marginally perpendicular to the applied pressure. By improving the contact interface in the vertical direction, that is, by realising the contact between the AM and the SE in a three-dimensional manner, it is expected that the charge/discharge characteristics of ASSBs can be improved even at low stack pressures.

Author Contributions

Y.S.and Y.O. conceived the study and conducted the operando X-ray CT experiments. H.Y. designed the operando measurement cell. Y.S. performed the charge/discharge test and analysed the X-ray CT data. A.T., M.U. and K.U. assisted with the use of beamline BL20XU and reconstruction processing. Y.S.and Y.O. wrote the manuscript with input from all authors.

Conflicts of interest

The authors declare no conflicts of interest associated with this manuscript.

Acknowledgements

This work was partially supported by JSPS KAKENHI Grant Number 19H02694, and the New Energy and Industrial Technology Development Organization (NEDO), JPNP20004. The synchrotron radiation experiments were performed at the BL20XU of SPring-8 with the approval of the Japan Synchrotron Radiation Research Institute (JASRI) (Proposal No. 2019B1726, 2020A0502, 2021A1005, 2021A1539, 2021B1724).

References

1. K. Takada, *Acta Mater.*, 2013, **61**, 759-770.
2. M. Klett, M. Giesecke, A. Nyman, F. Hallberg, R. W. Lindström, G. Lindbergh and I. Furó, *J. Am. Chem. Soc.*, 2012, **134**, 14654-14657.
3. S. A. Krachkovskiy, J. D. Bazak, P. Werhun, B. J. Balcom, I. C. Halalay and G. R. Goward, *J. Am. Chem. Soc.*, 2016, **138**, 7992-7999.
4. D. Takamatsu, A. Yoneyama, Y. Asari and T. Hirano, *J. Am. Chem. Soc.*, 2018, **140**, 1608-1611.
5. J. I. G. Dawkins, M. Z. Ghavidel, D. Chhin, I. Beaulieu, M. S. Hossain, R. Feng, J. Mauzeroll and S. B. Schougaard, *Anal. Chem.*, 2020, **92**, 10908-10912.
6. Y. Kato, S. Hori, T. Saito, K. Suzuki, M. Hirayama, A. Mitsui, M. Yonemura, H. Iba and R. Kanno, *Nat. Energy*, 2016, **1**, 7.
7. D. Cao, X. Sun, Q. Li, A. Natan, P. Xiang and H. Zhu, *Matter*, 2020, **3**, 57-94.
8. S. Yang, M. Takahashi, K. Yamamoto, K. Ohara, T. Watanabe, T. Uchiyama, T. Takami, A.

Sakuda, A. Hayashi, M. Tatsumisago and Y. Uchimoto, *Solid State Ionics*, 2022, **377**, 115869.
9. N. Kamaya, K. Homma, Y. Yamakawa, M. Hirayama, R. Kanno, M. Yonemura, T. Kamiyama, Y. Kato, S. Hama, K. Kawamoto and A. Mitsui, *Nat. Mater.*, 2011, **10**, 682-686.
10. Y. Orikasa, K. Yamamoto, T. Shimizu and Y. Uchimoto, *Chem. Phys. Rev.*, 2022, **3**, 011305.
11. Y. Orikasa, Y. Gogyo, H. Yamashige, M. Katayama, K. Chen, T. Mori, K. Yamamoto, T. Masese, Y. Inada, T. Ohta, Z. Siroma, S. Kato, H. Kinoshita, H. Arai, Z. Ogumi and Y. Uchimoto, *Sci. Rep.*, 2016, **6**, 26382.
12. W. Zhang, D. A. Weber, H. Weigand, T. Arlt, I. Manke, D. Schröder, R. Koerver, T. Leichtweiss, P. Hartmann, W. G. Zeier and J. Janek, *ACS Appl. Mater. Interfaces*, 2017, **9**, 17835-17845.
13. Y. J. Nam, D. Y. Oh, S. H. Jung and Y. S. Jung, *J. Power Sources*, 2018, **375**, 93-101.
14. Y. Kimura, M. Fakkao, T. Nakamura, T. Okumura, N. Ishiguro, O. Sekizawa, K. Nitta, T. Uruga, M. Tada, Y. Uchimoto and K. Amezawa, *ACS Appl. Energy Mater.*, 2020, **3**, 7782-7793.
15. J. M. Doux, Y. Y. C. Yang, D. H. S. Tan, H. Nguyen, E. A. Wu, X. F. Wang, A. Banerjee and Y. S. Meng, *J. Mater. Chem. A*, 2020, **8**, 5049-5055.
16. K. Chen, S. Shinjo, A. Sakuda, K. Yamamoto, T. Uchiyama, K. Kuratani, T. Takeuchi, Y. Orikasa, A. Hayashi, M. Tatsumisago, Y. Kimura, T. Nakamura, K. Amezawa and Y. Uchimoto, *J. Phys. Chem. C*, 2019, **123**, 3292-3298.
17. H. Fathiannasab, L. K. Zhu and Z. W. Chen, *J. Power Sources*, 2021, **483**.
18. G. Bucci, B. Talamini, A. Renuka Balakrishna, Y.-M. Chiang and W. C. Carter, *Phys. Rev. Mater.*, 2018, **2**, 105407.
19. T. Li, H. Kang, X. Zhou, C. Lim, B. Yan, V. De Andrade, F. De Carlo and L. Zhu, *ACS Appl. Mater. Interfaces*, 2018, **10**, 16927-16931.
20. S. Choi, M. Jeon, J. Ahn, W. D. Jung, S. M. Choi, J.-S. Kim, J. Lim, Y.-J. Jang, H.-G. Jung, J.-H. Lee, B.-I. Sang and H. Kim, *ACS Appl. Mater. Interfaces*, 2018, **10**, 23740-23747.
21. H. Fathiannasab, A. G. Kashkooli, T. Y. Li, L. K. Zhu and Z. W. Chen, *J. Electrochem. Soc.*, 2020, **167**.
22. A. Ohashi, M. Kodama, X. Y. Sun, S. Hori, K. Suzuki, R. Kanno and S. Hirai, *J. Power Sources*, 2020, **470**.
23. A. Ohashi, M. Kodama, N. Horikawa and S. Hirai, *J. Power Sources*, 2021, **483**.
24. J. M. Doux, H. Nguyen, D. H. S. Tan, A. Banerjee, X. F. Wang, E. A. Wu, C. Jo, H. D. Yang and Y. S. Meng, *Adv. Energy Mater.*, 2020, **10**.
25. C. Hansel and D. Kundu, *Adv. Mater. Interfaces*, 2021, **8**.
26. T. Hamann, L. Zhang, Y. H. Gong, G. Godbey, J. Gritton, D. McOwen, G. Hitz and E. Wachsman, *Adv. Funct. Mater.*, 2020, **30**.
27. J. Tippens, J. C. Miers, A. Afshar, J. A. Lewis, F. J. Q. Cortes, H. P. Qiao, T. S. Marchese, C. V. Di Leo, C. Saldana and M. T. McDowell, *Acs Energy Lett.*, 2019, **4**, 1475-1483.
28. S. Hao, J. J. Bailey, F. Iacoviello, J. F. Bu, P. S. Grant, D. J. L. Brett and P. R. Shearing, *Adv.*

Funct. Mater., 2021, **31**.
29. J. A. Lewis, F. J. Q. Cortes, Y. Liu, J. C. Miers, A. Verma, B. S. Vishnugopi, J. Tippens, D. Prakash, T. S. Marchese, S. Y. Han, C. Lee, P. P. Shetty, H. W. Lee, P. Shevchenko, F. De Carlo, C. Saldana, P. P. Mukherjee and M. T. McDowell, *Nat. Mater.*, 2021, **20**, 503-510.
30. M. Otoyama, M. Suyama, C. Hotehama, H. Kowada, Y. Takeda, K. Ito, A. Sakuda, M. Tatsumisago and A. Hayashi, *ACS Appl. Mater. Interfaces*, 2021, **13**, 5000-5007.
31. N. Seitzman, O. F. Bird, R. Andrykowski, S. Robbins, M. M. Al-Jassim and S. Pylypenko, *ACS Appl. Energy Mater.*, 2021, **4**, 1346-1355.
32. A. Neumann, S. Randau, K. Becker-Steinberger, T. Danner, S. Hein, Z. Y. Ning, J. Marrow, F. H. Richter, J. Janek and A. Latz, *ACS Appl. Mater. Interfaces*, 2020, **12**, 9277-9291.
33. N. Ohta, K. Takada, I. Sakaguchi, L. Zhang, R. Ma, K. Fukuda, M. Osada and T. Sasaki, *Electrochem. Commun.*, 2007, **9**, 1486-1490.
34. E. J. Cheng, K. Hong, N. J. Taylor, H. Choe, J. Wolfenstine and J. Sakamoto, *J. Eur. Ceram. Soc.*, 2017, **37**, 3213-3217.
35. D. A. Weber, A. Senyshyn, K. S. Weldert, S. Wenzel, W. Zhang, R. Kaiser, S. Berendts, J. Janek and W. G. Zeier, *Chem. Mater.*, 2016, **28**, 5905-5915.
36. L. Froboese, J. F. v. d. Sichel, T. Loellhoeffel, L. Helmers and A. Kwade, *J. Electrochem. Soc.*, 2019, **166**, A318-A328.
37. P. Minnmann, L. Quillman, S. Burkhardt, F. H. Richter and J. Janek, *J. Electrochem. Soc.*, 2021, **168**, 040537.
38. H. Fathiannasab, A. Ghorbani Kashkooli, T. Li, L. Zhu and Z. Chen, *J. Electrochem. Soc.*, 2020, **167**, 100558.
39. X. Lu, A. Bertei, D. P. Finegan, C. Tan, S. R. Daemi, J. S. Weaving, K. B. O'Regan, T. M. M. Heenan, G. Hinds, E. Kendrick, D. J. L. Brett and P. R. Shearing, *Nat. Commun.*, 2020, **11**, 2079.
40. A. Sakuda, A. Hayashi and M. Tatsumisago, *Sci. Rep.*, 2013, **3**, 2261.